Journal of Fluids and Structures (2001) **15,** 275–290
doi:10.1006/jfls.2000.0338, available online at http://www.idealibrary.com on IDEAL®

ON THE ADDED MASS AND DAMPING OF PERIODIC ARRAYS OF FULLY OR PARTIALLY POROUS DISKS

B. MOLIN

Ecole Supérieure d'Ingénieurs de Marseille, 13 451 Marseille cedex 20, France

(Received 27 March 2000, and in final form 17 August 2000)

Infinite and periodic arrays of porous disks are considered, in oscillatory flow perpendicular to their planes. This configuration is of interest for the offshore oil industry, for instance to be used as dampers to reduce the heave motion of truss SPAR platforms. The hydrodynamic problem is solved by the method of matched eigenfunction expansions, under the assumptions that losses of head, proportional to the square of the traversing velocities, occur at the disks, and that potential flow theory is applicable. Added mass and damping coefficients are derived, as functions of the relative spacings between the disks, and of the parameter $(A/a)\,(1-\tau)/(2\mu\tau^2)$, where A is the flow motion amplitude, a the disks radii, τ the porosity, or open-area ratio, and μ a discharge coefficient, close to 0.5. Results are also given for disks that are partially porous, from their axis to some radial distance. The practical applicability of the obtained results is discussed. © 2001 Academic Press

1. INTRODUCTION

OFFSHORE FLOATING OR COMPLIANT STRUCTURES are susceptible to resonant behaviour, under linear or nonlinear wave excitation. An efficient means to reduce the amplitudes of the resonant responses is to increase energy dissipation, by enhancing drag forces on some parts of the structures. A well-known example is the resonant roll motion of ships and barges, which bilge keels reduce efficiently. Another means is to shift the resonant frequencies outside the wave frequency range, for instance by increasing the added mass through additional plates.

In the past years some interest has arisen for perforated elements to be used as passive dampers [e.g. see Downie *et al.* 2000]. In 1990, the author (Molin & Legras 1990) proposed a hydrodynamic analysis of the Roseau tower stabilizer, an open box with slots. The theoretical model was based on potential flow theory and on the assumption that losses of head, proportional to the *square* of the (relative) traversing fluid velocities, are induced at the openings. Added mass and damping coefficients were obtained and good agreement was observed with experimental results from dedicated model tests [see also Damy & Molin (1991)]. A remarkable feature is that the added mass and damping are amplitude dependent. Other applications were subsequently considered, such as the heave motion of a semi-submersible platform with perforated pontoons (Molin 1992*a*, *b*), or the damping of waves through a series of vertical screens (Molin & Fourest 1992), or over a perforated horizontal plate (Molin & Bétous 1993; Molin 1999), within all cases there is good agreement between theoretical results and experiments. The case of steady current flow over shrouded cylinders was also investigated (Molin 1993).

An offshore production system that has gained some success, recently, is the SPAR platform, consisting in a floating vertical cylinder, of large draft [e.g. see Le Blanc (1996)]. The heave natural period is roughly equal to $2\pi\sqrt{d/g}$, d being the draft and g the

0889–9746/01/020275 + 16 $35.00/0

acceleration due to gravity. As a result, drafts over 200 m are necessary to ensure that the heave natural period be well beyond the wave period range. At smaller drafts, means to enhance damping are necessary. A proposed system consists in piling up a series of horizontal plates below the main hull, linked by a truss structure. The damping efficiency of such solid plates has been studied experimentally (Prislin *et al.*, 1998; Lake *et al.*, 1999). They also provide valuable supplementary added mass.

Another offshore structure is the TPG 3300 that consists in a deeply immersed flat pontoon, of large dimensions, supporting three or four vertical columns running through the free surface up to the deck (Thomas & Gaubil 1997). The pontoon is open in its centre, to permit passage for the risers. Being able to adjust the heave damping is an attractive issue that could make viable designs with reduced heave natural periods, as compared to the present ones. A possibility considered is to partially obstruct the opening through the pontoon, to reach an optimized open-area ratio.

These two cases have motivated the present study, where we consider an infinite and periodic series of disks. The disks are either completely or partially porous. The periodicity assumption renders the mathematical problem easier to tackle, and gives valuable results for several plates in proximity. For an isolated disk it suffices to increase the periodicity length beyond some distance. The circular disk assumption is also made for convenience: the geometry becomes axisymmetric.

The theoretical frame is identical with the one used in the quoted previous publications: use is made of potential flow theory. In the particular geometry considered here, this assumption is somewhat criticizable, since the flow separates not only through the openings but also at the edges of the disks. This latter effect is not taken into account in our theoretical frame. In the discussion part of the paper, we hint that it becomes negligible at sufficiently low values of the Keulegan–Carpenter number, expressed as $\mathrm{KC} = \pi A/a$, A being the motion amplitude and a the disk radius. It is for these small Keulegan–Carpenter numbers that porous disks appear as more efficient dampers than solid ones.

2. THEORY

2.1. Eigenfunction Expansions

We consider an infinite and periodic array of porous disks, with Oz as their axisymmetry axis; their radius is a, their spacing is l. The array is fixed. The fluid domain is unbounded. The flow velocity, far away from the array, is $W_0(t)$ in the Oz direction.

We use a cylindrical coordinate system (R, θ, z) with the plane $z = 0$ conciding with the porous disk number 0. We will specifically consider the cell number 1, in-between the porous disks 0 and 1 (extending from $z = 0$ up to l in z, and from 0 to a in R). Within this cell the velocity potential of the flow will be written as the sum of two eigenfunction expansions. We also use an eigenfunction expansion in the outer domain $R \geq a$.

In this outer domain the flow velocity is z-periodic with periodicity length l. The velocity potential is also antisymmetric in z with respect to each plane $z = jl$. Hence, it can be decomposed as

$$\varphi_e(R, z, t) = W_0(t)z + \sum_{n=1}^{\infty} A_n(t) \sin \lambda_n z \frac{\mathrm{K}_0(\lambda_n R)}{\mathrm{K}_0(\lambda_n a)}, \tag{1}$$

where $\lambda_n = 2n\pi/l$ and K_0 is the modified Bessel function of the second kind and order 0. With φ_e thus written, the Laplace equation and the condition at radial infinity are fulfilled.

In the inner domain, two sets of eigenfunctions are used. The first one corresponds to the

case when the disks are solid and the velocity potential satisfies the homogeneous Neumann condition. The expansion for φ_{iH} is then

$$\varphi_{iH}(R, z, t) = B_{0j}(t) + \sum_{m=1}^{\infty} B_m(t) \cos \mu_m z \frac{\mathrm{I}_0(\mu_m R)}{\mathrm{I}_0(\mu_m a)}, \tag{2}$$

where $\mu_m = (2m - 1)\pi/l$ and I_0 is the modified Bessel function of the first kind and order 0.

Only odd values of $\mu_m l/\pi$ are retained because of the antisymmetry property. Note that B_{0j} takes a different value in each cell. As a matter of fact one obtains readily that $B_{0j}(t) = W_0(t)(2j - 1)l/2$, where j is the cell number.

The second expansion is given in the following section, after the boundary condition at the porous walls has been described.

2.2. Boundary Condition at the Porous Walls

We use the same condition as in the quoted papers [e.g., see Molin (1992*b*)]. The porosity is assumed to consist of small openings, with sharp edges, so that the flow separates. There results a pressure drop, proportional to the square of the velocity through the opening:

$$\Delta P = \frac{1}{2\mu} \rho V |V|, \tag{3}$$

where μ is a discharge coefficient, the value of which depends on the shape of the openings and of the Reynolds number. In steady-flow conditions, typical values are in the range 0·5–1.

This relationship is then taken in an averaged sense, locally over a large number of openings. This means that the size and spacing of the openings must be much smaller than the scale of the averaged flow. The porosity (or open-area ratio) being τ, one writes that the pressure P applies on the solid parts (yielding a corrective factor $1 - \tau$), and that the velocity V is the (locally) averaged velocity v divided by τ. Hence, one gets

$$\Delta p = \frac{1 - \tau}{2\mu\tau^2} \rho v |v|, \tag{4}$$

where p is the (locally) averaged pressure, given by the Bernoulli–Lagrange equation

$$p = -\rho\varphi_t - \tfrac{1}{2}\rho(\nabla\varphi)^2. \tag{5}$$

The quadratic term can be discarded under the assumption that the motion amplitude of the flow be small as compared to the disk radius. (As a matter of fact, for the problem considered here, it can readily be checked that the velocities squared are the same on either side of the disks, so the quadratic terms just cancel out.)

Finally, the boundary condition at the disks is taken as

$$-\rho \frac{\partial}{\partial t}(\varphi^- - \varphi^+) = \rho \frac{1 - \tau}{2\mu\tau^2} \varphi_z |\varphi_z|, \tag{6}$$

φ^- is the velocity potential at the lower side of the disk, and φ^+ at the upper side.

It must be stressed out that the arguments leading to this equation are somewhat heuristic, and that some questions may be put forward with regard to the application of equation (3) to unsteady flows, or to the range of validity of (6) when the porosity ratio varies from zero to unity. Some choice also has to be made for the μ coefficient. To answer these questions comparisons with experimental results are necessary.

Such comparisons are reported in the quoted papers. They deal with various geometries and flow conditions, with porosity ratios in the range 10–40%. Quite favourable agreements between experimental and numerical results are reported, with the μ coefficient usually slightly above 0·5.

The second condition to impose at the disk results from mass conservation which requires that

$$\varphi_z^- = \varphi_z^+ = \varphi_z.$$

At the edge of the disk $\varphi^- = \varphi^+$ and hence the traversing velocity is nil. We take advantage of this to expand the traversing velocity, $\varphi_z(R, 0, t)$, as

$$\varphi_z(R, 0, t) = \sum_{i=1}^{\infty} C_i(t) \mathrm{J}_0(v_i R), \tag{7}$$

where J_0 is the Bessel function of order 0 and the 'wavenumbers' v_i are the roots of $\mathrm{J}_0(v_i a) = 0$. It can readily be verified (see Appendix A) that the functions $\mathrm{J}_0(v_i R)$ form an orthogonal set over the interval $[0\ a]$:

$$\int_0^a \mathrm{J}_0(v_i R)\mathrm{J}_0(v_j R) R \, \mathrm{d}R \equiv 0$$

for $i \neq j$. It can be checked that the set is complete.

When φ_z is thus given at $z = 0$ and l, a particular solution within the cell is

$$\varphi_{iP}(R, z, t) = \sum_{i=1}^{\infty} C_i(t) \frac{\cosh v_i z - \cosh v_i (z - l)}{v_i \sinh v_i l} \mathrm{J}_0(v_i R). \tag{8}$$

The general solution within the cell is obtained by adding up φ_{iH} and φ_{iP}:

$$\varphi_i(R, z, t) = B_{0j}(t) + \sum_{m=1}^{\infty} B_m(t) \cos \mu_m z \frac{\mathrm{I}_0(\mu_m R)}{\mathrm{I}_0(\mu_m a)} + \sum_{i=1}^{\infty} C_i(t) \frac{\cosh v_i z - \cosh v_i (z - l)}{v_i \sinh v_i l} \mathrm{J}_0(v_i R). \tag{9}$$

All that remains to be done is to match φ_i and φ_e, and their radial derivatives, for $R = a$, and use the discharge equation (6) as an evolution equation to advance the A_m, B_n and C_i coefficients in time, given the outer-flow velocity $W_0(t)$.

2.3. Matching of the Potentials

Setting $R = a$ in equations (1) and (9) we have

$$W_0(t) z + \sum_{n=1}^{\infty} A_n(t) \sin \lambda_n z = B_0(t) + \sum_{m=1}^{\infty} B_m(t) \cos \mu_m z. \tag{10}$$

Averaging each side in z over $[0\ l]$ we obtain $B_0 = W_0 l/2$.

Then we take advantage of the orthogonality of the set $[\cos \mu_m z]$ over $[0\ l]$. Multiplying each side by $\cos \mu_m z$ and integrating in z from 0 up to l we obtain the vectorial equation

$$\mathbf{B}(t) = \mathbf{B}_A \cdot \mathbf{A}(t) + W_0(t)\mathbf{D}, \tag{11}$$

where $\mathbf{B} = (B_1, B_2, \ldots, B_M)$, $\mathbf{A} = (A_1, A_2, \ldots, A_N)$, and the elements of the matrix $\mathbf{B}_A$ and vector $\mathbf{D}$ are

$$B_A(m, n) = \frac{8n}{\pi[4n^2 - (2m-1)^2]}, \qquad D(m) = -\frac{4l}{(2m-1)^2 \pi^2}. \tag{12}$$

2.4. Matching of the Radial Velocities

Equating the R derivatives of equations (1) and (9) at $R = a$ we get

$$\sum_{n=1}^{\infty} A_n(t) \sin \lambda_n z \, \lambda_n \frac{\mathrm{K}_0'(\lambda_n a)}{\mathrm{K}_0(\lambda_n a)} = \sum_{m=1}^{\infty} B_m(t) \cos \mu_m z \, \mu_m \frac{\mathrm{I}_0'(\mu_m a)}{\mathrm{I}_0(\mu_m a)} + \sum_{i=1}^{\infty} C_i(t) \frac{\cosh \nu_i z - \cosh \nu_i (z - l)}{\sinh \nu_i l} \mathrm{J}_0'(\nu_i a). \tag{13}$$

Now we take advantage of the orthogonality of the functions $[\sin \lambda_n z]$ over $[0\, l]$. Multiplying each side with $\sin \lambda_n z$ and integrating in z over $[0\, l]$ we obtain

$$\mathbf{A}(t) = \mathbf{A}_B \cdot \mathbf{B}(t) + \mathbf{A}_C \cdot \mathbf{C}(t), \tag{14}$$

where

$$A_B(n, m) = \frac{\beta_m}{\alpha_n} B_A(m, n), \qquad \alpha_n = \lambda_n \frac{\mathrm{K}_0'(\lambda_n a)}{\mathrm{K}_0(\lambda_n a)}, \qquad \beta_m = \mu_m \frac{\mathrm{I}_0'(\mu_m a)}{\mathrm{I}_0(\mu_m a)}, \tag{15}$$

$$A_C(n, i) = \frac{8n\pi}{4n^2\pi^2 + l^2 \nu_i^2} \frac{\mathrm{J}_1(\nu_i a)}{\alpha_n} \frac{\cosh \nu_i l - 1}{\sinh \nu_i l}. \tag{16}$$

Eliminating $\mathbf{A}$ between equations (11) and (14) we get

$$(\mathbf{I} - \mathbf{B}_A \cdot \mathbf{A}_B) \cdot \mathbf{B}(t) = W_0(t)\mathbf{D} + \mathbf{B}_A \cdot \mathbf{A}_C \cdot \mathbf{C}(t), \tag{17}$$

where $\mathbf{I}$ is the unit matrix.

2.5. Discharge Equation

The jump of potential at the plate is

$$\varphi(0^+) - \varphi(0^-) = W_0(t) l + 2 \sum_{m=1}^{M} B_m(t) \frac{\mathrm{I}_0(\mu_m R)}{\mathrm{I}_0(\mu_m a)} + 2 \sum_{i=1}^{I} C_i(t) \frac{1 - \cosh \nu_i l}{\nu_i \sinh \nu_i l} \mathrm{J}_0(\nu_i R). \tag{18}$$

The discharge equation takes the form

$$\dot{W}_0(t) l + 2 \sum_{m=1}^{M} \dot{B}_m(t) \frac{\mathrm{I}_0(\mu_m R)}{\mathrm{I}_0(\mu_m a)} + 2 \sum_{i=1}^{I} \dot{C}_i(t) \frac{1 - \cosh \nu_i l}{\nu_i \sinh \nu_i l} \mathrm{J}_0(\nu_i R) = \frac{1 - \tau}{2\mu\tau^2} |\varphi_z| \varphi_z. \tag{19}$$

This time we take advantage of the orthogonality of the $[\mathrm{J}_0(\nu_i R)]$ functions over $[0\, a]$. Multiplying each side with $\mathrm{J}_0(\nu_i R)\, R$ and integrating in R from 0 to a we get

$$\dot{\mathbf{C}}(t) = \mathbf{C}_B \cdot \dot{\mathbf{B}}(t) + \dot{W}_0(t) \mathbf{E}_0 + \mathbf{E}_F \cdot \mathbf{F}(t), \tag{20}$$

where

$$C_B(i, m) = \frac{2}{a \mathrm{J}_1(\nu_i a)} \frac{\nu_i^2}{\nu_i^2 + \mu_m^2} \frac{\sinh \nu_i l}{\cosh \nu_i l - 1}, \tag{21}$$

$$E_0(i) = \frac{l}{a \mathrm{J}_1(\nu_i a)} \frac{\sinh \nu_i l}{\cosh \nu_i l - 1}, \tag{22}$$

$$E_F(i, j) = -\frac{1 - \tau}{2\mu\tau^2} \frac{1}{a^2 \mathrm{J}_1^2(\nu_i a)} \frac{\sinh \nu_i l}{\cosh \nu_i l - 1} [R_{j+1} \mathrm{J}_1(\nu_i R_{j+1}) - R_j \mathrm{J}_1(\nu_i R_j)], \tag{23}$$

and $F(j)$ is the averaged value of $\varphi_z\,|\varphi_z|$ over the interval $[R_j\ R_{j+1}]$. The radius a has been discretized in N_{pt} segments $[R_j\ R_{j+1}]$ to permit a numerical evaluation of the integral

$$\int_0^a \mathrm{J}_0(\nu_i R)\left|\sum_{i=1}^{\infty} C_i(t)\mathrm{J}_0(\nu_i R)\right|\left[\sum_{i=1}^{\infty} C_i(t)\mathrm{J}_0(\nu_i R)\right] R\,\mathrm{d}R. \tag{24}$$

2.6. Integration in Time

Taking the time derivative of equation (17) and making use of equation (20) to eliminate $\dot{\mathbf{C}}$ we obtain

$$(\mathbf{I} - \mathbf{B}_A \cdot \mathbf{A}_B - \mathbf{B}_A \cdot \mathbf{A}_C \cdot \mathbf{C}_B) \cdot \dot{\mathbf{B}}(t) = \dot{W}_0(t)(\mathbf{D} + \mathbf{B}_A \cdot \mathbf{A}_C \cdot \mathbf{E}_0) + \mathbf{B}_A \cdot \mathbf{A}_C \cdot \mathbf{E}_F \cdot \mathbf{F}(t). \tag{25}$$

This equation, together with equation (20) permits to advance in time $\mathbf{B}(t)$ and $\mathbf{C}(t)$, the outer velocity $W_0(t)$ being given in time. They are all taken equal to 0 at time $t = 0$ so that equation (17) be fulfilled. The matrix $(\mathbf{I} - \mathbf{B}_A \cdot \mathbf{A}_B - \mathbf{B}_A \cdot \mathbf{A}_C \cdot \mathbf{C}_B)$ is calculated and inverted prior to the simulation.

2.7. Partly Solid Disk

In this section we consider the case of a partly porous, partly solid disk: the porous part extends from $R = 0$ to a_P, the solid part from $R = a_P$ to a.

This extension has been motivated by the case of the TPG 3300 pontoon, which consists of a flat triangular plate with a central square opening. It is not precisely an axisymmetric geometry but it is expected that the circular case can give valuable results to optimize the porosity ratio of the central opening, in order to maximize the heave damping at resonance.

The only modification that has to be made, with regard to the theory already developed, is that the no-flow condition must be enforced at the disk, from $R = a_P$ to a:

$$\sum_{i=1}^{I} C_i(t)\mathrm{J}_0(\nu_i R) = 0 \qquad \text{for } a_P \le R \le a, \tag{26}$$

while the discharge equation still holds from $R = 0$ to a_P:

$$\sum_{i=1}^{I} \dot{C}_i(t)\gamma_i \mathrm{J}_0(\nu_i R) = \dot{W}_0(t) l + 2\sum_{m=1}^{M} \dot{B}_m(t)\frac{\mathrm{I}_0(\mu_m R)}{\mathrm{I}_0(\mu_m a)} - \frac{1-\tau}{2\mu\tau^2}\,|\varphi_z|\varphi_z, \tag{27}$$

where $\gamma_i = 2(\cosh \nu_i l - 1)/(\nu_i \sinh \nu_i l)$.

Dividing both sides of equation (27) by γ_k, and differentiating equation (26) in time, gives

$$\sum_{i=1}^{I} \dot{C}_i(t)\frac{\gamma_i}{\gamma_k}\,\mathrm{J}_0(\nu_i R) = \frac{1}{\gamma_k}\,\dot{W}_0(t) l + \frac{2}{\gamma_k}\sum_{m=1}^{M} \dot{B}_m(t)\frac{\mathrm{I}_0(\mu_m R)}{\mathrm{I}_0(\mu_m a)} - \frac{1}{\gamma_k}\frac{1-\tau}{2\mu\tau^2}\,|\varphi_z|\varphi_z \tag{28}$$

for $0 \le R \le a_P$, and

$$\sum_{i=1}^{I} \dot{C}_i(t)\mathrm{J}_0(\nu_i R) = 0 \tag{29}$$

for $a_P \le R \le a$.

Again we multiply each side of both equations by $\mathrm{J}_0(\nu_k R)R$, we integrate them over their respective domains of validity and we add up side by side. We obtain

$$\dot{C}_k(t)\int_0^a \mathrm{J}_0^2(\nu_k R)R\,\mathrm{d}R + \sum_{i\ne k} \dot{C}_i(t)\left(1 - \frac{\gamma_i}{\gamma_k}\right)\int_{a_P}^{a} \mathrm{J}_0(\nu_i R)\mathrm{J}_0(\nu_k R)R\,\mathrm{d}R$$

$$= \frac{\dot{W}_0(t)l}{\gamma_k}\int_0^{a_P} \mathrm{J}_0(v_k R)R\,\mathrm{d}R + \frac{2}{\gamma_k}\sum_{m=1}^{M}\dot{B}_m(t)\int_0^{a_P}\frac{\mathrm{I}_0(\mu_m R)\mathrm{J}_0(v_k R)}{\mathrm{I}_0(\mu_m a)}R\,\mathrm{d}R$$

$$-\frac{1}{\gamma_k}\frac{1-\tau}{2\mu\tau^2}\int_0^{a_P}\mathrm{J}_0(v_k R)|\varphi_z|\,\varphi_z R\,\mathrm{d}R \tag{30}$$

or, in vectorial form,

$$\mathbf{I}_P\cdot\dot{\mathbf{C}}(t) = \mathbf{C}_{B_P}\cdot\dot{\mathbf{B}}(t) + \dot{W}_0(t)\mathbf{E}_{0\mathrm{P}} + \mathbf{E}_{F_P}\cdot\mathbf{F}(t). \tag{31}$$

Inverting the matrix $\mathbf{I}_P$, the same procedure as in the previous case can be used.

3. RESULTS

3.1. Solid Disks

First we consider the case of fully solid disks. In such case the problem reduces to equation (17) where $\mathbf{C} \equiv \mathbf{0}$. Once this linear system is solved, with $W_0(t) = 1$, the added mass M_a is readily derived as

$$M_a = \rho\pi\left[la^2 + 4a\sum_{m=1}^{M} B_m\frac{\mathrm{I}_1(\mu_m a)}{\mu_m\mathrm{I}_0(\mu_m a)}\right]. \tag{32}$$

Figure 1 gives the added mass coefficient $C_a = M_a/(\rho a^3)$ as a function of the ratio a/l. When the relative spacing goes to infinity ($a/l \to 0$), the case of one single disk $C_a = \frac{8}{3}$ is recovered. When the relative spacing goes to zero, the added mass should reduce to the mass of the entrapped water: $M_a = \rho\pi a^2 l$ giving $C_a \simeq \pi l/a$. This asymptotic behaviour is well recovered by our numerical results.

For these calculations the truncation orders M and N of the expansions 1 and 2 were taken equal to 100.

Now we investigate the rate of convergence with respect to the truncation order. This is shown in Figure 2, which gives the added mass coefficient for $l/a = 2$ and 10 versus $1/M$ (N being taken equal to M). It can be seen that convergence is quicker for $l/a = 2$.

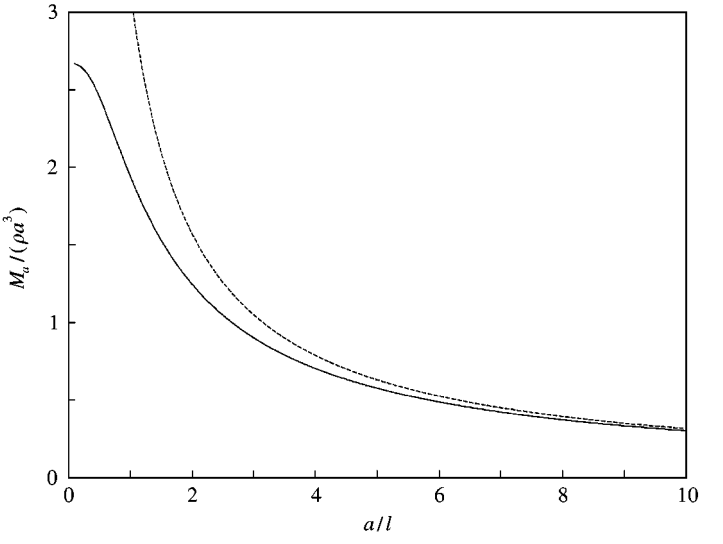

Figure 1. Solid disk. ——, Added mass coefficient as a function of a/l; – – –, $\pi l/a$.

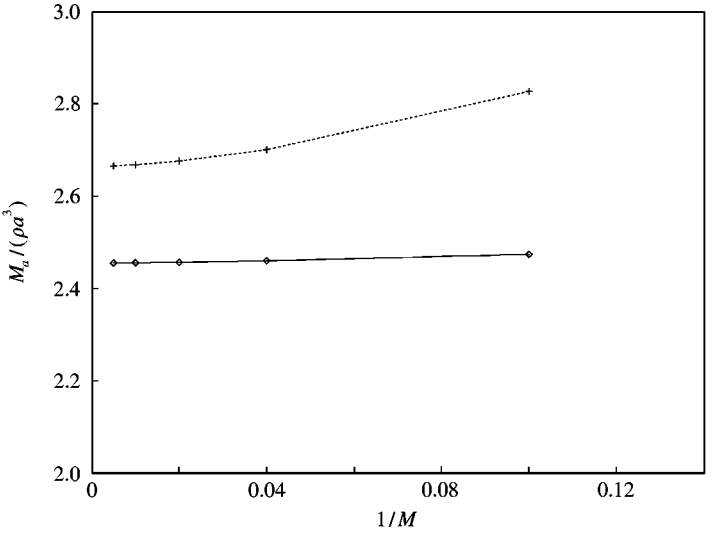

Figure 2. Solid disk. Added mass coefficient as a function of $1/M$: ——, $l/a = 2$; – – –, $l/a = 10$.

3.2. Porous Disks

Now we consider the case of fully porous disks. The outer velocity $W_0(t)$ is taken as

$$W_0(t) = A\omega \sin \omega t,$$

and equations (20) and (25) are integrated in time (with a Predictor–Corrector method), with $\mathbf{B}(0) = \mathbf{C}(0) = \mathbf{0}$.

First, we consider a spacing l/a equal to 2, and a nondimensional outer fluid motion amplitude $A/a(1 - \tau)/(2\mu\tau^2)$ equal to 1·5. All truncation orders M, N and I are chosen equal to 100 and the number of segments used to calculate the integral (24) is taken as 200.

Figure 3 shows the simulated hydrodynamic force (made nondimensional) on the disk, obtained via integration of the pressure differential, together with the nondimensional outer fluid velocity ($\sin \omega t$) and outer fluid acceleration ($\cos \omega t$). It can be observed that a steady state is very quickly attained, within less than one period. For this particular amplitude, the maximum of the force is reached right in-between the maxima of the outer velocity and acceleration: the damping and added mass coefficients are about equal. These are obtained by Fourier-analyzing the force over one period. In this case, we obtain 1·247 for the added mass coefficient C_a and 1·175 for the damping coefficient C_b, defined through

$$F(t) = \rho a^3 (C_a \dot{W}_0(t) + \omega C_b W_0(t)) = \rho a^3 A\omega^2 (C_a \cos \omega t + C_b \sin \omega t),$$

where $F(t)$ is the hydrodynamic force.

In Figure 3, from time $t/T = 2{\cdot}5$ the outer flow velocity and acceleration are made equal to zero. The hydrodynamic force then decreases smoothly to zero, meaning that the flow kinematics persist for some time: the discharge equation (6) introduces memory effects into the flow.

As a check that the discharge equation (6) is fulfilled, we show in Figure 4 its left- and right-hand sides, when $t/T = 1{\cdot}88$ and 2·10, that is, when the hydrodynamic force is nil and at its maximum. At either instant the two curves are nearly indistinguishable. It can be observed that when the force is nil, the pressure drop is not equal to zero everywhere along the radius. It just changes sign at $R/a \sim 0{\cdot}75$.

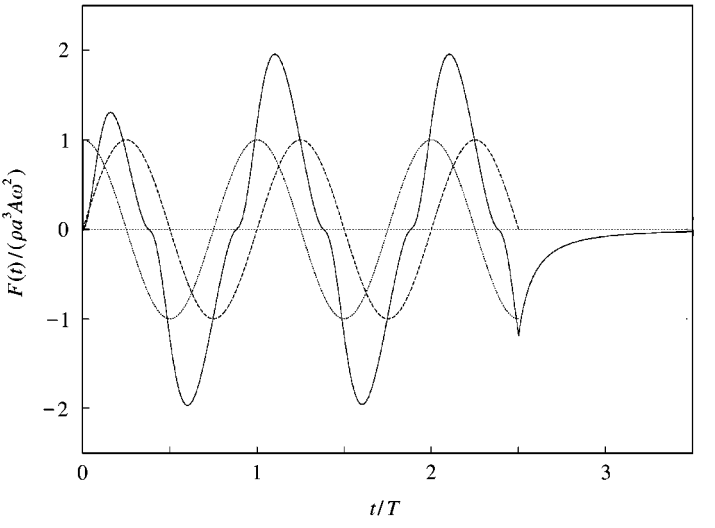

Figure 3. Porous disk in sinusoidal flow. ——, Simulated hydrodynamic force $F(t)$ (normalized by $\rho a^3 A\omega^2$) versus nondimensional time t/T; – – – –, $\sin(\omega t)$; ----, $\cos(\omega t)$.

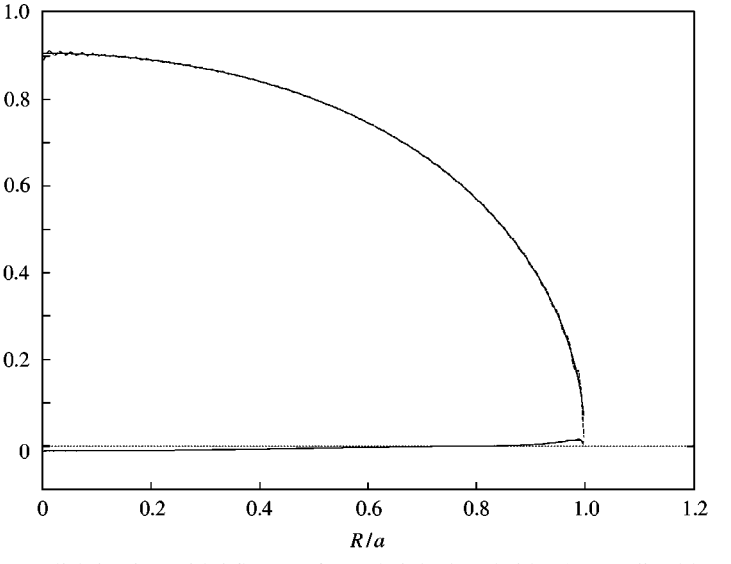

Figure 4. Porous disk in sinusoidal flow. Left- and right-hand sides (normalized by $\rho aA\omega^2$) of the discharge equation (6) at two different instants: ——, left-hand side; ----, right-hand side.

We now give the added mass and damping coefficients, when the parameter $(A/a)(1-\tau)/(2\mu\tau^2)$ varies from zero up to ten. They are given in Figures 5–7 for $l/a = 1, 2$ and 5 (results for $l/a > 5$ differ little from this latter case).

When the parameter $(A/a)(1-\tau)/(2\mu\tau^2)$ goes to zero both the added mass and damping coefficients become nil: the water particles flow freely through the porous wall. When it increases to infinity, the solid disk results are asymptotically recovered, with the damping coefficient going to zero and the added mass one increasing up to its value given in Figure 1. For a value of $(A/a)(1-\tau)/(2\mu\tau^2)$ somewhere in-between 1 and 1·5 (for the relative spacings considered here) the damping coefficient reaches its peak value. It can be observed that it is

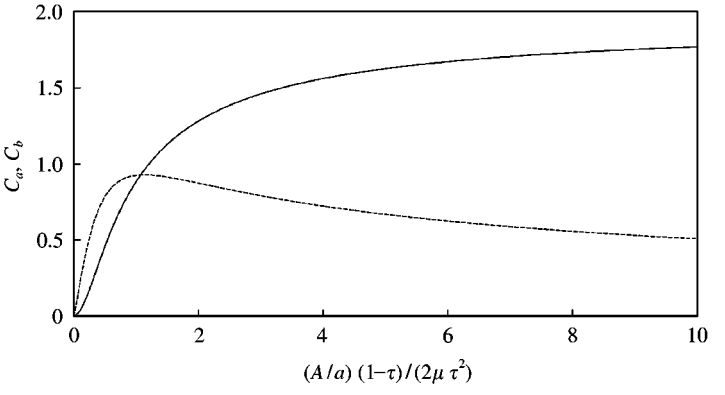

Figure 5. Porous disk in sinusoidal flow. Relative spacing $l/a = 1$. Added mass and damping coefficients versus $(A/a)(1 - \tau)/(2\mu\tau^2)$: ——, added mass coefficient C_a; -----, damping coefficient C_b.

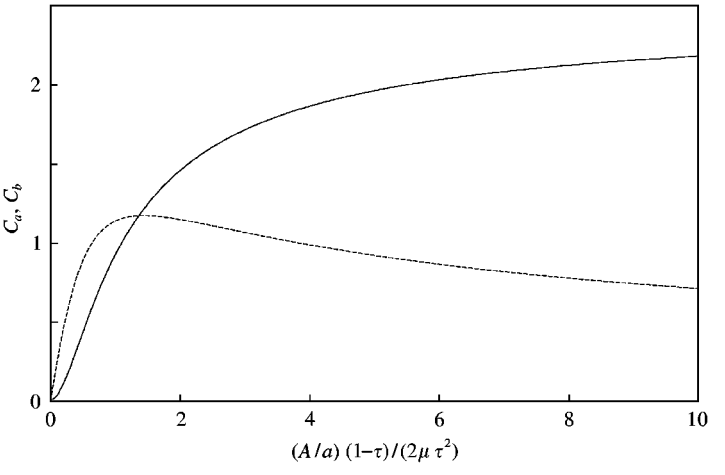

Figure 6. Porous disk in sinusoidal flow. Relative spacing $l/a = 2$. Added mass and damping coefficients versus $(A/a)(1 - \tau)/(2\mu\tau^2)$: ——, added mass coefficient C_a; – – –, damping coefficent C_b.

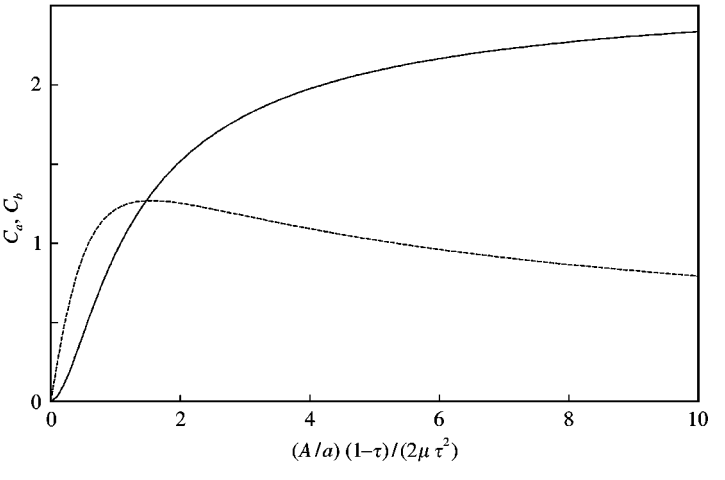

Figure 7. Porous disk in sinusoidal flow. Relative spacing $l/a = 5$. Added mass coefficient (——) and damping coefficient (– – –) versus $(A/a)(1 - \tau)/(2\mu\tau^2)$.

then equal to the added mass coefficient, that is the hydrodynamic force is 45° out of phase with the flow acceleration. Similar features are obtained with porous circular cylinders (Molin 1992*b*). Another remarkable result, also obtained with porous cylinders and with 2-D plates (Molin 2000), is that the peak value of the damping coefficient is always equal, or very close, to half the value of the added mass coefficient in the limit $(A/a)(1-\tau)/(2\mu\tau^2) \to \infty$, that is for the solid case.

Coming now to the effect of relative spacing, it can be seen from Figures 5–7 that, when l/a varies from 1 to 5, the peak value of the damping coefficient increases by less than 40%. To maximize the damping effect over a given length, it is thus preferable to install many plates.

3.3. Partly Porous Partly Solid Disks

Now, we consider the case of disks which are porous from their axis to some radial distance a_P and then solid from a_P to a. This introduces a new geometric parameter a_P/a. As written above, the incentive is to obtain results relevant for the pontoon of the TPG 3300. Hence, we assume the disks to be far apart: we only consider the case $l/a = 5$.

First, we present some results in one particular case $a_P/a = 0{\cdot}5$ and $(A/a)(1-\tau)/(2\mu\tau^2) = 0{\cdot}5$ (which, from Figure 10, corresponds with the maximum of the damping coefficient). In Figure 8, we show the z component of the velocity (normalized by $A\,\omega$) along the radius, at five different instants separated by one-tenth of a period, starting at $t = T$. As already noticed for the fully porous disks, the phasing of the traversing velocity varies with R/a. It can be checked that the no-flow condition is well verified on the solid part. In Figure 9, we show the pressure drop at the same instants.

In Figures 10 and 11 we show the added mass and damping coefficients, plotted against the parameter $(A/a)(1-\tau)/(2\mu\tau^2)$, for $a_P/a = 0{\cdot}5$ and $0{\cdot}75$. When the obtained damping coefficients are related to the fully porous case, it can be seen that for $a_P/a = 0{\cdot}5$ (that is a porous area equal to one-fourth the total disk area), the maximum damping coefficient is about 60% of the maximum damping of the fully porous one. For $a_P/a = 0{\cdot}75$ (56·25% of

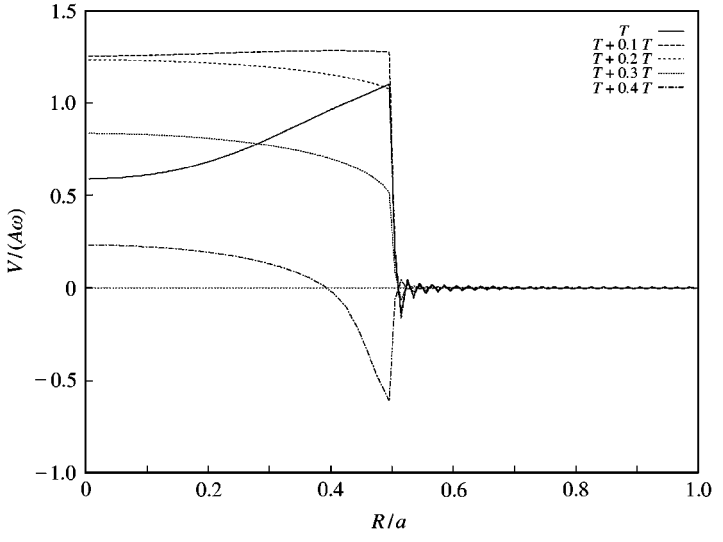

Figure 8. Partly porous partly solid disk in sinusoidal flow. Traversing velocity $V/(A\omega)$ along the radius at different instants. Relative spacing $l/a = 5$. Radius ratio $a_P/a = 0{\cdot}5$.

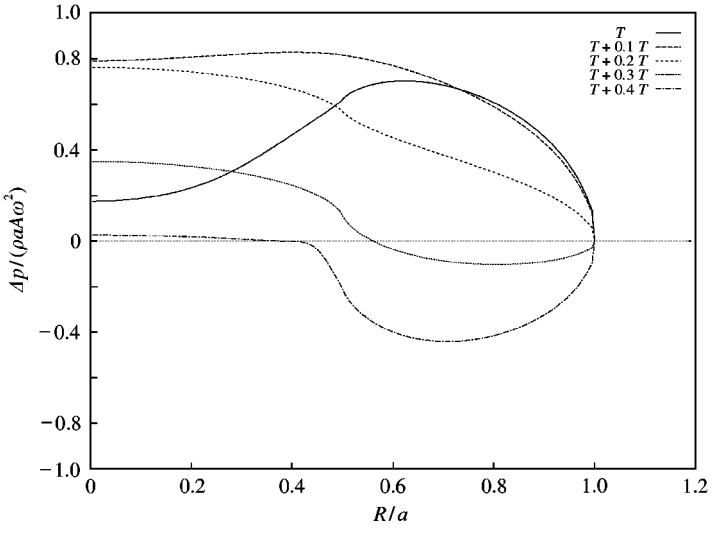

Figure 9. Partly porous partly solid disk in sinusoidal flow. Pressure differential $\Delta p/(\rho a A \omega^2)$ along the radius at different instants. Relative spacing $l/a = 5$. Radius ratio $a_P/a = 0{\cdot}5$.

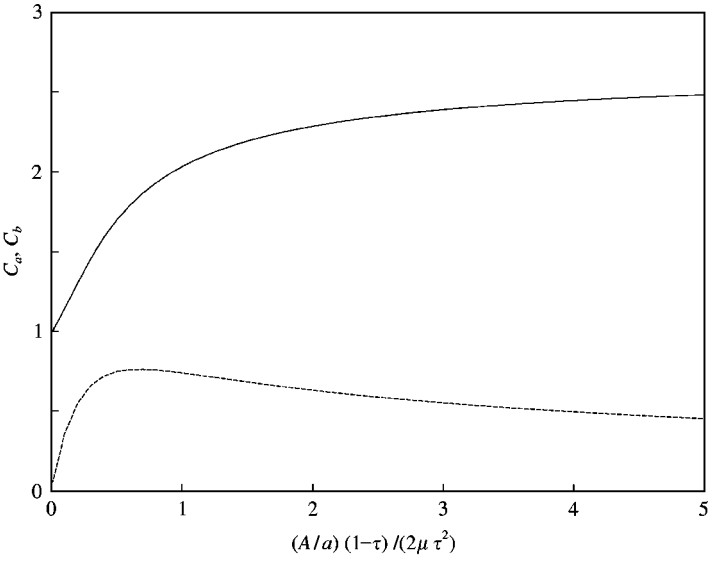

Figure 10. Partly porous partly solid disk in sinusoidal flow. Added mass (C_a) and damping (C_b) coefficients versus $(A/a)(1-\tau)/(2\mu\tau^2)$. Relative spacing $l/a = 5$. Radius ratio $a_P/a = 0{\cdot}5$: ——, C_a; – – –, C_b.

the area), the ratio is 85%. This is because blockage effects strongly enhance the flow velocity through the porous part.

4. DISCUSSION

Our theoretical approach, based on perfect fluid and irrotational flow assumptions, predicts no damping for a solid disk. Practically however, the flow separates at the edge, inducing drag forces and energy dissipation. With a porous disk, there is separation at the edge as

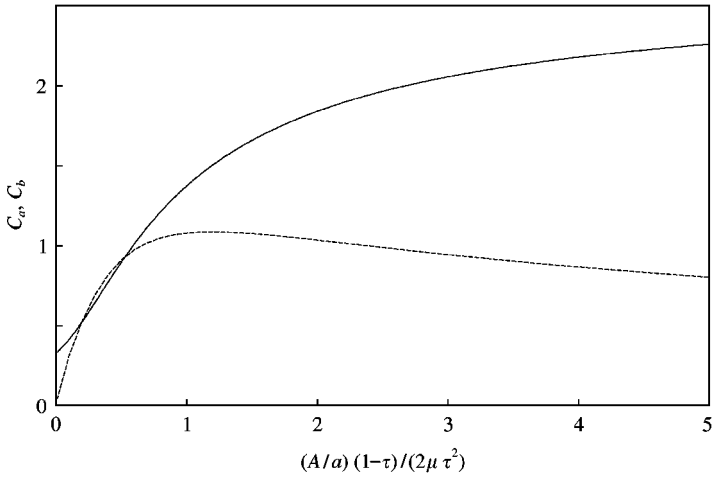

Figure 11. Partly porous partly solid disk in sinusoidal flow. Added mass (——) and damping (– – –) coefficients versus $(A/a)(1-\tau)/(2\mu\tau^2)$. Relative spacing $l/a = 5$. Radius ratio $a_P/a = 0{\cdot}75$.

well, and also separation through the openings. Our theoretical model takes the latter effect into account (in a somewhat idealized way), but not the former one. One feels intuitively that our model may yield appropriate values for the damping in so far as the effect of separation through the openings is dominant with regard to the effect of separation at the edge. A way to check whether this can be the case is to compare the damping values that we obtain for a porous disk with available experimental values of the damping for a solid disk. If the porous disk damping exceeds the solid disk damping by far, then there is a chance that our model could be of some value.

Experimental data for solid disks are provided by Lake *et al.* (1999). They obtain that the damping coefficient varies linearly with the Keulegan–Carpenter number KC, for $0{\cdot}1 \leq KC \leq 0{\cdot}5$. From their figure 5, one has, roughly :

$$B' = 0{\cdot}25\mathrm{KC}, \quad \text{where } B' = \frac{3B}{16\rho a^3\omega}, \quad \mathrm{KC} = \pi\,\frac{A}{a}.$$

Referring to our Figure 7, we see that with an optimized porosity ratio, the damping coefficient $B/(\rho a^3\omega)$ is equal to about 1·25. Hence, the ratio (optimized porous damping)/(solid damping) is given by

$$\frac{B_{\text{porous}}}{B_{\text{solid}}} \simeq 0{\cdot}95\mathrm{KC}^{-1}.$$

When the KC number is larger than one, no extra damping can be gained by making the disk porous. There is little point in wondering whether our theory is applicable or not. One has to better keep the disks solid.

The matter becomes different if the KC number is much smaller than one. For SPAR platforms it has been considered to add up solid plates to the truss structure below the hull, in order to increase the damping in heave. Typically, the SPAR radius is around 15 m and the motion amplitude is small, of the order of 1 m. This means a KC number around 0·2, assuming the plates radii to be equal to the SPAR radius. Then there is a lot to gain by making the plates porous. With a porosity slightly below 20%, the heave damping can be increased by a factor 4 or 5. This result would demand confirmation through dedicated model testing.

In Molin & Legras (1990) a somewhat similar situation is encountered. The structure considered is a truncated, open-ended, vertical cylinder, initially designed to increase the horizontal added mass of compliant towers. Forced oscillation tests are reported on different models, of height and diameter both equal to 1 m, at KC numbers ranging from nearly zero up to about 0·5. Porosity ratios of 10, 20 and 24% were achieved, either as horizontal slots (12 over the height of the cylinder) or with small circular perforations. It was found that the measured and calculated damping coefficients agreed closely at the smallest porosity ratio, for KC numbers ranging from zero up to the value associated with the peak in the damping curve. At larger KC numbers they started to deviate from each other, the experimental values remaining more or less constant while the numerical ones decreased slowly. This discrepancy was attributed to the drag forces taking place at the lower and upper sharp edges of the truncated cylinder.

Another remarkable result obtained here is the sensitivity of the added mass coefficient of a porous disk to the porosity ratio and Keulegan–Carpenter number. It may also look surprising that the added mass becomes nil when the KC number goes to zero. For the perforated truncated cylinder considered in Molin & Legras (1990) this behaviour was confirmed by the experimental results. In that case, the radius of the circular perforations was equal to 1 mm, to be compared with a cylinder diameter of 1 m and motion amplitudes being as small as 2 mm. In the slotted version, owing to the larger spacings in-between the slots, the added mass coefficient did not quite decrease to zero as the motion amplitude was reduced, but it nevertheless became very small, amounting to only about 10% of the zero porosity case.

The sensitivity of the added mass coefficient with the motion amplitude offers interesting perspectives when one is concerned with resonance problems. They are discussed in Molin (1992*b*) in the particular case of semi-submersible platforms with slotted pontoons.

ACKNOWLEDGEMENTS

The incentive to work on this problem was provided through discussions with Prof. J.M.R. Graham of Imperial College, and with Ph. Weber of Technip.

REFERENCES

DAMY, G. & MOLIN, B. 1991 Stabilizers for compliant towers: numerical and experimental studies. In *Proceedings Brasil Offshore'91*, *Rio de Janeiro*.

DOWNIE, M. J., GRAHAM, J. M. R. & WANG, J. 2000 The effectiveness of porous damping devices. In *Proceedings 10th International Offshore and Polar Engineering Conference (ISOPE)*, Vol. III, pp. 418–425, Seattle.

LAKE, M., HE, H., TROESCH, A. W., PERLIN, M. & THIAGARAJAN, K. P. 1999 Hydrodynamic coefficient estimation for TLP and SPAR structures. In *Proceedings 18th International Conference on Offshore Mechanics and Arctic Engineering (OMAE)*, paper 4103, St. John's. Newfoundland, Canada.

LE BLANC, L. 1996 Spar-shaped drilling unit designed for 8,000–10,000 ft depth corridor. *Offshore* **56,** 30–31.

MOLIN, B. 1992*a* A new small semi concept for marginal fields. In *Proceedings 24th Offshore Technology Conference*, paper 7050, Houston, Texas, U.S.A.

MOLIN, B. 1992*b* Motion damping by slotted structures. In *Hydrodynamics: Computations, Model Tests and Reality, Developments in Marine Technology,* Vol. 10, pp. 297–303. Dordrecht: Elsevier.

MOLIN, B. 1993 A potential flow model for the drag of shrouded cylinders. *Journal of Fluids & Structures* **7,** 29–38.

MOLIN, B. 1999 Numerical and physical tanks. Making them fit, 22nd Memorial Georg Weinblum Conference, Hamburg (to appear in *Ship Technology Research*).

MOLIN, B. 2000 Added mass and damping of two-dimensional porous plates, Unpublished note.

MOLIN, B. & LEGRAS, J.-L. 1990 Hydrodynamic modelling of the Roseau tower stabilizer. In *Proceedings 9th International Conference on Offshore Mechanics and Arctic Engineering (OMAE)*, *Houston*, *TX*, *U.S.A.* Vol I, Part B, pp. 329–336.

MOLIN, B. & FOUREST, J.-M. 1992 Numerical modeling of progressive wave absorbers. In *Proceedings 7th International Workshop on Water Waves & Floating Bodies*, pp. 199–203, Val de Reuil, France.

MOLIN, B. & BÉTOUS, P. H. 1993 Atténuation de la houle par une dalle horizontale immergée et perforée. In *Actes des Quatriémes Journées de l'Hydrodynamique*, pp. 387–400, Nantes, France (in French).

PRISLIN, I., BLEVINS, R. D. & HALKYARD, J. E. 1998 Viscous damping and added mass of solid square plates. In *Proceedings 17th International Conference on Offshore Engineering and Arctic Engineering (OMAE)*, Lisbon, Portugal.

THOMAS, P. A. & GAUBIL, F. 1997 From the TPG 500, production drilling quarter jack-up to the TPG 3300, semi-submersible platform for deep water. In *Proceedings 29th Offshore Technology Conference*, *Houston*, *TX*, *U.S.A.*, paper 8564.

APPENDIX A: INTEGRALS

A.1. ORTHOGONALITY OF THE $J_0(v_iR)$ FUNCTIONS OVER $[0\ a]$

Let $u(R) = J_0(v_iR)$ and $v(R) = J_0(v_jR)$ with $v_i \neq v_j$; u and v satisfy the differential equations

$$Ru'' + u' + v_i^2 Ru = 0,$$

$$Rv'' + v' + v_j^2 Rv = 0.$$

Multiplying both sides of the first equation with v, both sides of the second one with u, and subtracting them, one gets

$$\frac{\partial}{\partial R}[R(u'v - uv')] + (v_i^2 - v_j^2)Ruv = 0,$$

Hence

$$(v_i^2 - v_j^2)\int_0^a uvR\,\mathrm{d}R = -R(u'v - uv')\Big|_0^a = 0$$

if $u(a) = v(a) = 0$.

A.2. INTEGRAL $\int_0^a J_0^2(v_iR)R\,\mathrm{d}R$

One may readily check that

$$\frac{\partial}{\partial z}\left\{\frac{z^2}{2}(J_0^2(z) + J_1^2(z))\right\} = zJ_0^2(z).$$

Since $J_0(v_ia) \equiv 0$, this leads to

$$\int_0^a J_0^2(v_iR)R\,\mathrm{d}R = \frac{a^2}{2}J_1^2(v_ia)$$

A.3. INTEGRAL $\int_0^a I_0(\mu_mR)J_0(v_iR)R\,\mathrm{d}R$

Be $u(R) = J_0(v_iR)$ and $v(R) = I_0(\mu_mR)$. They verify

$$Ru'' + u' + v_i^2 Ru = 0,$$

$$Rv'' + v' - \mu_m^2 Rv = 0.$$

Multiplying the first equation with v, the second one by u, subtracting, and integrating, gives

$$\int_0^a Ruv \, dR = \frac{1}{v_i^2 + \mu_m^2} R(uv' - u'v)\Big|_0^a.$$

One obtains finally

$$\int_0^a I_0(\mu_m R) J_0(v_i R) R \, dR = \frac{a v_i}{v_i^2 + \mu_m^2} J_1(v_i a) I_0(\mu_m a).$$